防蝕工程　第十九卷第三期　第369　388頁　2005年9月
Journal of Chinese Corrosion Engineering, Vol.19 No.3, PP. 369~388 (2005)

低合金鋼在大氣環境下的腐蝕抗性與機械性質

陳彥羽*[1]、施漢章[1]、鄭暉志[2]、魏豐義[2]、王立華[3]、翁榮洲[3]

Corrosion Resistance and Mechanical Properties of Low-Alloy Steels under Atmospheric Conditions

Y. Y. Chen*[1], H. C. Shih[1], H. J. Tzeng[2], L. I. Wei[2], L. H. Wang[3], J. C.Oung[3]

摘 要

本研究利用實驗室的加速乾濕循環試驗，將四種新發展出來的低合金鋼與一碳鋼 (SS400) 及一耐候鋼 (Acr-Ten A) 在含氯鹽環境下 (5wt.% NaCl) 的腐蝕抗性與機械強度加以比較。這四種新的低合金鋼分別標號為 1604A、1604B、1605A 與 1605B。結果發現：經過 72 週期的循環腐蝕測試後，六種鋼對腐蝕的敏感度由高至低依序為：SS400 > Acr-Ten A > 1604B ≥ 1604A > 1605B ≥ 1605A。而因腐蝕造成機械特性的改變以 SS400 為最少，Acr-Ten A 次之，其他四種鋼再次之且差異不大。最後，每一種鋼的銹層特性均以 SEM 觀察之，並以 FTIR 與 EPMA 作分析比較。結果顯示：在大多數鋼表面上所形成的銹層均由較鬆散的外銹層與一緻密的內銹層所組成。每一種鋼材的外銹層又是由 α-FeOOH、γ-FeOOH、磁鐵礦 (Fe_3O_4)、水、和非晶質的氫氧化鐵 ($FeO_x(OH)_{3-2x}$, x = 0-1) 所構成；另一方面，內銹層則主要由磁鐵礦與少量的 α-FeOOH 所組成。此外，本研究還發現合金添加物中的銅元素在銹層與基材的介面處富集；而鉻元素則在銹層中聚集。最後，綜合加速試驗與銹層分析的結果顯示：1605A 與 1605B 低合金鋼在潮濕並含鹽分的環境下，其耐候性質較 Acr-Ten A 為佳。

關鍵詞：大氣腐蝕；耐候鋼；加速試驗；重量損失；銹層；FTIR；EPMA。

1 國立清華大學材料科學與工程學系
Department of Materials Science and Engineering, National Tsing Hua University.
2 中國鋼鐵股份有限公司公司
China Steel Corporation
3 工業技術研究院工業材料研究所
Materials Research Laboratories, Industrial Technology Research Institute.
* 連絡作者(franklin_chen_1@hotmail.com)

ABSTRACT

The corrosion resistance and mechanical strength of four newly developed low-alloy steels (LAS) were compared with a carbon steel (SS400) and a weathering steel (Acr-Ten A) using a laboratory-accelerated test that involved cyclic wet/dry conditions in a chloride environment (5wt.% NaCl). The new LAS were designated 1605A, 1605B, 1604A, and 1604B. After 72 cycles of cyclic corrosion tests, the susceptibility of the steels to corrosion could be listed in the following order based on their weight loss (from high to low) : SS400 > Acr-Ten A > 1604B ≥ 1604A > 1605B ≥ 1605A. The change in mechanical properties by corrosion was the least for SS400, Acr-Ten A was second, and effects of corrosion on the mechanical properties of the other four low alloy steels were similar. Finally, the characteristics of the rust layers on each LAS sample were observed by SEM, and analyzed by FTIR and EPMA. The results indicated that most of the rust layers on the test steels were composed of a loose outer rust layer and a dense inner rust layer. The outer rust layer of each steel was composed of α-FeOOH, γ-FeOOH, magnetite (Fe_3O_4), H_2O, and amorphous ferric oxyhydroxide ($FeO_x(OH)_{3-2x}$, x = 0-1), while the inner rust layer was composed mainly of Fe_3O_4 with a little α-FeOOH. In addition, it was apparent that the copper and chromium alloying additions were enriched, respectively, at the rust-layer/substrate interface and in the rust layers. Finally, combining the results of the accelerated tests and the rust layer analysis showed that low alloy steels, such as 1605A and 1605B, have better weathering steel properties than Acr-Ten A for use in the humid and salty weather.

Keywords: Atmospheric corrosion; weathering steel; accelerated test; weight loss; rust layer; FTIR; EPMA.

1. Introduction

The most common types of damage that occur to structural steels during their lifetime are fatigue and rusting. Except for stainless steels, which are more costly, almost no uncoated ferrous products can resist the influences of various corrosion factors coming from the atmosphere, e.g. sulfide, chloride, dust, and moisture. However, weathering steel (WS) is a kind of steel that can be maintained for dozens of years at low cost and without coating. It is well known that the enhanced corrosion resistance of weathering steel results from the formation of a compact protective, i.e. tightly adherent, rust layer. This protective rust layer will gradually become denser over time and will isolate the steel from various corrosion factors and so reduce the rate of corrosion substantially. In previous studies, the formation of the protective rust layer was shown to be related to the alloying elements (e.g. Cr, P, Cu, Ni, etc.) and to the environmental conditions [1-7]. Due to its numerous advantages, WS has potential application in the civil engineering and automobile industries. For example, they are employed in the construction of buildings and bridges and for architectural trim without the necessity of painting, thereby saving appreciable maintenance costs over the life of the structure. Therefore, it makes sense to tailor WS alloys for specific environments and substitute them for the less corrosion-resistant common steels wherever applicable.

The development of weathering steels dates back to the 1930s and they have been used widely since then because of their unique corrosion

resistance [8, 9]. In the 1950s, a WS called Cor-Ten A [8-11] was developed in North America. Its outstanding corrosion resistance is suitable for the North American continental climate, but it doesn't perform as well in the semi-tropical monsoon climate of an island with high humidity and salinity. The seasonal monsoons bring large amounts of sea salt, and even the higher levels of air pollution can contribute to more aggressive conditions for corrosion. For this reason, it is necessary to develop different types of WS that are suitable locally.

Although the real-life exposure test provides the most reliable information on atmospheric corrosion of metals, it is rather time-consuming. However, laboratory accelerated tests produce useful data in a short time and are profitable in assessing the durability of metals in certain specific atmospheres [7].

In principle, atmospheric corrosion is primarily ascribed to electrochemical processes occurring on a metallic surface under wet/dry conditions. Consequently, it is likely that most, if not all, corrosion results from liquid-phase reactions [12]. Cyclic wet/dry conditions and Cl^- concentration are important controlling parameters in accelerated tests. According to numerous studies using accelerated tests [6, 7, 13-15], the rust layers formed on WS are less protective than those on carbon steel (CS) under continuously wet conditions such as when they are buried in soil or totally immersed in water; however, the intermittent wet/dry process facilitates the formation of a protective rust layer in WS that enhances its corrosion resistance. Therefore, a cyclic salt spray and ultraviolet lighting are used to simulate the intermittent wet/dry corrosion environment in chloride-containing atmospheres. Also, the difference between the mechanical and electrochemical properties before and after the accelerated tests are frequently measured.

Generally speaking, the corrosion products on the surface of WS are mainly α-FeOOH, γ-FeOOH, β-FeOOH, $Fe(OH)_3$, and Fe_3O_4. These products can coexist partly as crystalline and partly as amorphous structures [6, 14]. When the steel contacts moisture and corrodes, the initial corrosion product is mainly γ-FeOOH, but gradually this transforms to α-FeOOH as a result of the intermittently wet/dry conditions [6, 14]. The alloying additions in WS result in corrosion products that are denser and more stable than those on CS. Although α-FeOOH and γ-FeOOH can also be observed in corrosion products on CS, they are porous in nature since they are not enhanced by the alloying elements, and, in addition, the adhesion is poor between the rust layer and the substrate. Consequently, the corrosive species can readily penetrate the porous rust layers to the substrate where corrosion reactions may proceed endlessly. It is apparent that the rust layers on CS provide little or no protection to the substrate.

In this study, we compared the atmospheric corrosion resistance (weathering resistance) of four low-alloy steels (LAS) that were developed by China Steel Corp., with two other alloys (SS400 and Acr-Ten A) to identify the alloying elements that confer additional corrosion resistance and/or mechanical strength. We also investigated the mechanical properties after these accelerated tests. Finally, we analyzed the morphology, bonding nature, and chemistry of the rust products using SEM, FTIR, and EPMA, respectively.

2. Experimental Procedures

2.1 Test Materials

Four LAS, designated 1604A, 1604B, 1605A, and 1605B, were compared with the commercial high-phosphorus WS (Acr-Ten A) and CS (SS400). The chemical compositions were analyzed by

an inductively coupled plasma-atomic emission spectrometer (ICP-AES) and are listed in Table 1. The coiling temperature of 1605B was 400°C, but the other three steels were coiled at 600°C. The test materials were all cut into reduced plate tensile specimens, 6.25mm in width, for the accelerated laboratory tests according to ASTM E 8M-98 [16]; specimen dimensions are shown in Figure 1. Figures 2(a)-2(e) show the surface microstructures of the four as-received low-alloy steels and Acr-Ten A. They were all first mechanically wet ground using a 1500 grit SiC paper and then etched in a Nital solution (97% nitric acid + 3% alcohol) for ~ 20s. The microstructures of 1604A (Figure 2(a)) and 1604B (Figure 2(b)), as shown by SEM, are both of pure ferrite; 1605A (Figure 2(c)) and Acr-Ten A (Figure 2(e)) are duplex structures consisting of ferrite and small amounts of pearlite; and 1605B (Figure 2(d)) is composed of ferrite and bainite.

2.2 Alternating Wet/Dry Accelerated Corrosion Tests

Prior to the accelerated cyclic corrosion tests, all the surfaces of the tensile specimens were polished using 600-grade emery paper, cleaned ultrasonically in acetone, and then rinsed with distilled water before drying in air. All specimens were put simultaneously into the salt spray tester (Q.U.V. Accelerated Weathering Tester) and were mounted at 30° to the horizontal according to the ASTM G 50-76 specification for simulating natural atmospheric corrosion [17]. The accelerated corrosion testing procedure involved cycling between a dry environment and a mist composed of 5 wt.% (~0.86M) NaCl, according to ASTM B 117-97 [18]. Each wet/dry cycle (24 h) consisted of a wetting period (8 h at 35°C, 97 ± 1% RH) plus a drying period (16 h at 60°C, 20% RH). The lighting source was an UVB-313 tube. The dry/wet ratio was 2:1, which was more severe than conditions in a previous study (drying period for 18h and wetting period for 6h) [19]. This was done to determine whether the differences between WS and CS would be more significant than those under the dry/wet ratio of 3:1 if the time of wetness increased during the 24h cycle. On the other hand, the chamber temperature during the drying period was raised from 50°C [19] to 60°C in order to increase the density of the rust layers [20]. NaCl was provided only during the wetting period, and the NaCl concentration in the chamber was controlled to 5M. The accelerated corrosion tests lasted for a total of 72 cycles.

2.3 Mechanical Properties and Weight Loss Measurements

After some pre-determined numbers of testing (e.g. 18 cycles and 45 cycles), the tensile specimens were taken out and pulled to failure in a tensile testing machine (Material Testing System 810). The strain rate was set at 0.1 mm/s. The load and elongation were measured continuously by a load cell and electric dial gauge, respectively, the outputs of which were recorded on a computer-controlled X-Y recorder (YEW MODEL 3025) until fracture occurred. The stress-strain curves were used to determine the yield strength (YS), the ultimate tensile strength (UTS), and the elongation (%). The results were then plotted versus the number of corrosion cycles to compare the steels tested.

In preparation for weight-loss measurements after the specimens fractured, corrosion products on the specimen surfaces were removed chemically by immersion in a Clark's solution (100ml HCl, sp gr 1.19 + 20g Sb_2O_3 +50g $SnCl_2$) [21] that was vigorously stirred for ~10 min at 25°C. After corrosion products had been completely removed, the specimens were

rinsed with distilled water, dried in air, and then weighed to determine their weight loss.

2.4 Rust Products, Observation and Analysis

Throughout the accelerated corrosion tests, the specimens were examined without stripping the rust from the surface. The surface and cross-section of the rust layers were analyzed using various analytical techniques, including scanning electron microscopy (SEM), Fourier transform infrared spectroscopy (FTIR) and electro probe microanalysis (EPMA). Special case was taken to analyze the interface between the steel substrate and its rust layer, and to understand the distribution of the alloying elements at this interface.

3. Results and Discussion

3.1 Weight Loss

Almost all of the rust layers fell off the tensile specimens as they were being pulled to failure by the MTS 810. The remaining rust was removed by immersing the specimens into Clark's solution and vigorously stirring. The rust-free specimens were then weighed. The results of the relation between weight loss and the test cycles are listed in Figure 3. The weight loss data in this study are expressed as the weight loss per unit surface area. In general, the final weight losses are the lowest for 1605A and 1605B, and the highest for SS400. Therefore, the alloys can be arranged in order of decreasing weight loss, as follows: SS400 (pearlite/ferrite) > Acr-Ten A (pearlite/ferrite) > 1604B (ferrite) ≥ 1604A (ferrite) > 1605B (bainite/ferrite) ≥ 1605A (pearlite/ferrite). It is found that the corrosion resistance of steels containing higher chromium and silicon, such as 1605A and 1605B, need a longer time (> 30 cycles) to reveal their corrosion resistance. In other words, the corrosion rate of 1605A and 1605B in accelerated tests decreased markedly after ~30 cycles. This means that, under these severe cyclic wet/dry test conditions, a longer time is necessary to form adhesive dense rust layers on high-chromium steels, e.g. 1605A, 1605B. A similar phenomenon was observed for Acr-Ten A, but its weathering resistance was less significant than 1605A and 1605B under this environment. On the other hand, for 1604A and 1604B (without Cr), the corrosion rates did not decrease with time. This may be explained by the fact that the dense inner-rust layer didn't appear to adhere tightly to the substrate. The adhesion of rust layers will be discussed later. The lowest weight loss occurred in 1604A and 1604B at earlier stages of accelerated corrosion (e.g., < 50 cycles) is probably because of their pure ferrite microstructure associated with their low carbon content [7, 13]. Finally, the corrosion (weight loss) rate of the common carbon steel (SS400) containing low chromium didn't decrease with an increase in the number of test cycles.

The results in Figure 3 have been re-plotted in Figure 4 using log-log (bi-logarithm) coordinates to reveal a linear relationship between log (weight loss) and log (test cycles) [19]. Atmospheric corrosion of WS and CS in the accelerated test followed the well-known bi-logarithmic equation:

$$\text{Log } W = \text{Log } X + Y \text{ Log } t \quad \text{or} \quad W = X \times t^{Y} \qquad (1)$$

Where W is the weight loss (mg/cm^2), t is the exposure time (test cycles), and X and Y are constants. Since X is equal to W when time is unity (t = 1), X is considered a measure of the initial corrosion resistance of the metal. On the other hand, Y reflects the change of weight loss with exposure time. Table 2 gives values of the constants

in Equation (1). From Table 2, it can be seen that the Y values for 1605A (1.0636) and for 1605B (1.0239) are roughly consistent with the previous observations that the corrosion (weight loss) rates for both LASs decrease as time increases. For neutral atmospheric corrosion, the value of Y should not exceed 1. However, it is apparent that the Y values here are > 1. The constant Y approaches 0.5 when an ideal diffusion process is the controlling mechanism. Y values > 0.5 result from an acceleration of the diffusion process when the rust is detached by cracking, erosion, dissolution, etc. Conversely, Y values < 0.5 arise from a decrease in the diffusion coefficient as the rust layer becomes more and more compact with time. The reason for Y actually being > 1 may be that the ratio of wet period/dry period is not optimum. The drying period (16 h) is only twice as long as the wetting period (8 h), and a longer drying time may be necessary to allow for the moist and salty rust layers to become completely dry. In addition, it is possible that the weight loss increases with an increase in the number of test cycles because the presence of thicker rust layers will make it more difficult to dry the surface of the steel. Table 2 shows the X and Y coefficients for the six steels. Also, the difference between the results shown in Figure 3 and Table 2 for 1605A and 1605B can be explained by the fact that, for a greater number of test cycles, the protective effect of tightly adhesive rust layers outweighs the negative effect of the rust layers absorbing water. Furthermore, the weathering effect becomes more significant as the number of cycle increases.

The values of X and Y obtained from actual exposure tests in the atmosphere can be used to predict the atmospheric corrosion behavior over a longer period of time [22, 23]. However, there are still some differences between actual atmospheric exposure and the laboratory simulation test. In an accelerated corrosion test, the environmental variables are more restricted than those of the actual atmosphere in a real life situation. X and Y values are mainly influenced by the chloride concentration, temperature, and the wet/dry period ratio in a salt spray test.

3.2 Effects of Corrosion on the Mechanical Properties

After the accelerated cyclic corrosion testing, all the tensile specimens were pulled to failure in a MTS 810 machine to measure their mechanical properties. Figures 5 and 6 show that the mechanical strength (YS and UTS) of the steels decreases with an increase in the number of test cycles. The decrease in YS and UTS is the smallest for SS400. Interestingly, the YS and UTS for Acr-Ten A decrease quite linearly with an increase of the number of test cycles. On the other hand, the changes of the other four LAS are less regular, but decrease in general. These non-linear reductions in mechanical strength may be due to the negative effect of the surface roughness on the mechanical properties.

In Figure 5, it is apparent that the yield strengths of 1604A, 1604B, 1605A, and 1605B are higher than those of Acr-Ten A and SS400. Furthermore, the YS of 1605A and 1605B are higher than 1604A and 1604B. The strengthening effects are due to the addition of manganese (1604A/B and 1605A/B) and chromium (1605A/B). Manganese will combine with sulfur to form globular MnS and it also strengthens the ferrite in steels by solid-solution strengthening. On the other hand, chromium will combine with carbon in steel to form carbides and also strengthen the steels. Because 1605A and 1605B contain both Cr and Mn, they have higher mechanical strength than the other test steels.

The changes in mechanical strength, while

near linear, are scattered and insufficient data were accumulated to determine linear regression curves, such as $S = X \times t^{Y}$, that express the variation in strength with the number of test cycles [24], similar to Figure 4. Therefore, we compared the mechanical strength and the weight loss of each steel after 45 cycles, as shown in Table 3. It is apparent that the reduction in the mechanical strength, especially of the yield strength, is greater than that of the cross-sectional area. Only the mechanical strength (YS and UTS) ratios for SS400 approach the value of remaining cross-section ratio. This may be attributed to the fact that the loosely adhering rust layers on the substrate of SS400 provide no local protection, so almost uniform corrosion occurred on the substrate thereby maintaining a smooth surface. The smoother surface of SS400 after 45 cycles provided less chance of stress concentration than the rougher surfaces developed on the other alloys. The larger decrease in the YS and UTS for the latter alloys may also be due to localized corrosion such as pitting.

Figure 7 illustrates the relationship between elongation and test period. It shows that elongation decreases with an increase in the number of test cycles, but that decreases are not linear. However, after 20 cycles, the elongations of 1605A and 1605B are not changed much. In addition, the ductility of the alloys are roughly 70% ~ 82% of their original values.

3.3 Analysis of the Rust Layers

The cross-sections of each steel after 18 and after 45 cycles of accelerated tests were observed by SEM, as shown in Figures 8(a)-8(h). It shows that the rust layers in these test steels all contain voids and/or micro-cracks, which facilitate the penetration of the chloride solution to the substrate, which, in turn, promotes the corrosion process. Most of the rust layers on the test steels were composed of two parts: the loose outer rust layer and the dense inner rust layer. After 18 cycles, the corrosion resistances of 1604A and 1604B are better than that of SS400, because the rust layers are denser and the voids and micro-cracks are fewer. The rust products on the two LAS (1604A/B) are similar to SS400 -- in that they can be removed easily from the substrate. The thickness of the rust layers on 1604A and 1604B after 18 test cycles are 100-200μm thinner than that on SS400 (~400μm). On the other hand, the corrosion resistances of 1605A, 1605B, and Acr-Ten A are inferior to SS400 after 18 cycles. This is probably due to the fact that the drying time was not long enough in the cases of the adherent, dense, and deep-colored inner rust layers of the three LAS, thereby exposing the substrates of these steels to humid condition for longer periods of time, and allowing more corrosion. The superior corrosion resistance of SS400 at this stage (18 cycles) is caused by the gap (separation) between the rust layer and the substrate (Figure 8(a)). This loose rust layer can easily be removed leaving the substrate basically untouched in a dry condition. In addition, it is difficult to transport chloride across the gap between the rust layer and the substrate. For those two reasons, the corrosion weight loss of SS400 was lower after longer test cycles (18-45 cycles).

After the accelerated tests were finished (45 cycles), the rust layers of SS400 were still easily removed and contained numerous voids. However, although most of the rust layer separated from the substrates of 1604A and of 1604B, parts of each rust layer did adhere, allowing localized corrosion, which made the substrate rougher than that of SS400. Furthermore, there were deep-colored inner rust layers found at the rust-layer/substrate interfaces of 1605A, 1605B, and Acr-Ten A. This indicates that the rust layers of these three LASs gradually

form the thick (400-500μm) and dense inner rust layers during the later cycles of the test. Experience with the stripping process and SEM observations suggested that the degree of difficulty in removing rust layers is dependent on the amount of chromium in the steels. The rust layers on the low-alloy steels with high-chromium content, such as 1605A, 1605B, and Acr-Ten A, are more compact and more difficult to remove. The dense, crack-free rust layers on Acr-Ten A and 1605A after 45 cycles are shown in Figure 8(d) and 8(h), respectively.

3.4 Composition and Structure of the Rust

The composition of the rust layers after 18 cycles and after 45 cycles was analyzed using FTIR. The outer rust layers of each steel were quite similar after 18 and 45 cycles, and were composed of α-FeOOH, γ-FeOOH, magnetite (Fe_3O_4), H_2O, and amorphous ferric oxyhydroxide ($FeO_x(OH)_{3-2x}$, x = 0-1), as shown in Figures 9(a) and 9(d). After stripping off the outer rust layers, the inner rust layers were analyzed, which showed that the main absorption peak for γ-FeOOH became weaker (Figures 9(b) and 9(e)). For Acr-Ten A, 1605A, and 1605B, almost no γ-FeOOH was found in the surface rust layer (Figures 9(c)). The surface rust layer means that the rust layer just covers above the substrate (~50μm thick), and the inner rust layer is just under the outer rust layer.

These observations can be explained by acknowledging that the γ-FeOOH was transformed into other kinds of corrosion products; for example, much of the γ-FeOOH on WS was transformed into α-FeOOH after 45 cycles of the exposure in the experiment. Misawa et al. proposed that dissolved chromium and phosphorus ions enhance the formation of uniform amorphous ferric oxyhydroxide, which protects the steel substrate, and that this amorphous ferric oxyhydroxide will further transform into the more stable and protective structure of α-FeOOH [25,26]. However, the presence of Cl^- would lead to facile metal dissolution ($Fe \rightarrow Fe^{2+} + 2e^-$) by depassivating the iron surface. The acidic nature of the hydrated Fe^{2+} cation dissociates and therefore lowers the local pH via the following reaction:

$$Fe(H_2O)_6^{2+} \rightarrow Fe(H_2O)_5(OH)^+ + H^+ \quad (2)$$

This may promote the phase transformation to amorphous ferric oxyhydroxide ($FeO_x(OH)_{3-2x}$, x = 0-1) and α-FeOOH. After 45 cycles in the cyclic corrosion test, the compact rust layers on the substrate of 1605A, 1605B, and Acr-Ten A were composed largely of Fe_3O_4 with a little of α-FeOOH (Figure 9(c)). The valence of Fe in Fe_3O_4 is 8/3, which indicates that the dense rust layers prevent the diffusion of oxygen and result in the incomplete oxidation of Fe.

Rust forms on steel in air, which in the case of plain carbon steel does not provide protection, whereas it does on weathering steel, so the rusting rate tends to decrease [27,28]. In water containing dissolved oxygen, the following anodic and cathodic reactions occur:

$$\text{Anodic:} \quad Fe \rightarrow Fe^{2+} + 2e^- \quad (3)$$

$$\text{Cathodic:} \quad 1/2O_2 + H_2O + 2e^- \rightarrow 2OH^- \quad (4)$$

$$\text{Overall:} \quad Fe + 1/2O_2 + H_2O \rightarrow Fe(OH)_2 \quad (5)$$

Rust is formed by the further oxidation of $Fe(OH)_2$ with water:

$$2Fe(OH)_2 + 1/2O_2 + H_2O \rightarrow 2Fe(OH)_3 \quad (6)$$

Some researchers have drawn conclusions about the corrosion mechanisms from the rust

compositions. For instance, some work indicates that γ-FeOOH forms first and is then transformed to γ-FeOOH and Fe_3O_4 [29-31]. Rust becomes rich in Fe_3O_4 but low in γ-FeOOH in coastal regions whereas rust formed in inland regions is rich in α-FeOOH. On the other hand, Evans [32] assumed that the dissolution of iron ($Fe \rightarrow Fe^{2+} + 2e^-$) occurs at the substrate-Fe_3O_4 interface and that a cathodic reaction ($6FeOOH + 2e^- \rightarrow 2Fe_3O_4 + 2H_2O + 2OH^-$) occurs at the Fe_3O_4/FeOOH interface. It was assumed that the reaction $Fe^{3+} \rightarrow Fe^{2+}$ occurs in the rust.

It must be noted that none of the FTIR examinations demonstrated the existence of β-FeOOH. This may be explained by the fact that the absorption band of β-FeOOH is wide and is affected by the absorption bands of other ferric oxides and hydroxides due to the smaller quantity of β-FeOOH. Therefore, the absorption band of β-FeOOH cannot be observed. In addition, Misawa et al. [25] proposed that an inner cohesive protective rust film is formed on low-alloy steels after long-term atmospheric exposure (industrial or urban). The protective film consists of amorphous δ-FeOOH, the formation of which is catalyzed by copper and phosphorus of the steel surface; alternate drying and wetting favors development of its protective qualities. Keiser et al. [33] confirmed that the typical inner adherent rust layer consists mostly of δ-FeOOH. However, it was not possible to determine whether δ-FeOOH existed or not in this study because the absorption band of δ-FeOOH is similar to that of amorphous ferric oxyhydroxide.

Examination of the cross-sections of the rust layers by EPMA showed the distributions of alloying elements for Acr-Ten A (Figure 10) and 1605A (Figure 11). The rust layer in Acr-Ten A was enriched in chromium but contained no manganese, as shown in Figure 10(b). Furthermore, the interface was not obviously enriched in copper but copper was concentrated in the rust layer near the interface (Figure 10(c)). In addition, the substrate was rich in silicon. On the other hand, the distributions of alloying elements in the rust are roughly the same for 1605A and 1605B. Chromium and silicon were abundant in the inner rust layer of 1605A and 1605B after 45 cycles under the experimental conditions, as shown in Figure 11(c). By contrast, copper concentrated at the interface between the rust layer and the substrate, while manganese decreased markedly from the interface to the rust layer, and seemed to disappear completely in the rust layer, as shown in Figure 11(b).

In the research on weathering steels, several methods for increasing the corrosion resistance are described. For instance, one way is to alloy the steel with elements such as chromium, copper, and phosphorus, which enhance the densification and adhesion of the rust layers leading to better protection against corrosion. Another method is to lower the carbon content of the steels in order to reduce the strain energy and the amount of Fe_3C produced thereby increasing the corrosion resistance of the steel [7, 13]. Alternatively, the addition of titanium combined with some substitutional elements, like carbon and nitrogen, can achieve the effect of lowering the strain energy of weathering steels [34].

As indicated above, chromium in WS plays an important role in enhancing the compactness, densification, and adhesion of the rust layers, thereby decreasing the diffusion of oxygen to the substrate. Furthermore, chromium can reduce the conductivity of the rust layers [35]. From the present EPMA analyses, it was found that chromium was gradually enriched in the rust layers (Figure 11(c)), and that the dark regions in the rust layers were enriched with chromium while the light regions were chromium-depleted, as shown in Figure 11(a).

Under the severe wet/dry cyclic conditions in the present experiment, the Cr-rich dark inner rust layers were formed incompletely. As a result of the poor protection by the rust layers, serious corrosion of the substrate occurred.

Copper alloying additions may segregate during the dissolution of iron, and may adsorb on the surface of the steel, and so accelerate the uniform dissolution of the steel [35-37]. On the other hand, copper will promote rust formation in the early stage of exposure, then will enrich the rust layers resulting in beneficial effects similar to those of chromium, i.e. of enhancing the protection and densification of the rust layers. In the present study, copper only concentrated obviously at the interface, which had little effect in promoting the protectiveness of the rust layers.

In addition, it is generally believed that manganese has no significant contribution in enhancing the weathering resistance of WS because of the absence of manganese in the rust layers, and that silicon should help to increase the corrosion resistance [24]. This can be confirmed by the fact that silicon was rich in the rust layers of both 1605A and 1605B, as shown in Figure 11(c). However, the amount of silicon in the rust layer of Acr-Ten A was low (Figure 10(c)). It is therefore concluded that silicon alloying additions may be helpful to enhance the protection and densification of the rust layers for 1605A and 1605B, and therefore their corrosion resistance is better than that of the common used WS (Acr-Ten A) even the C, Cu and Cr compositions (which appear to be most influential in determining corrosion resistance) of Acr-Ten A are almost identical to 1605A/B.

Finally, the results of the accelerated tests indicate that the corrosion rates tend to decrease with an increase in the number of test cycles for 1605A and 1605B, similar to the behavior of Acr-Ten A. In addition, the mechanical strength of 1605A and 1605B are maintained after long periods of intermittent wet/dry corrosion testing. Furthermore, the rust layers on the two low-alloy steels have protective inner rust layer like Acr-Ten A. Therefore, it may be concluded that 1605A and 1605B are weathering steels seem to be more suitable for use in the humid and salty weather than Acr-Ten A.

4. Conclusions

The following points summarize the results of this study:

1. The results of the chloride cyclic corrosion tests indicated that the susceptibility of the steels to corrosion can be listed in the following order based on their weight loss (from high to low): SS400 (pearlite/ferrite) > Acr-Ten A (pearlite/ferrite) > 1604B (ferrite) ≥ 1604A (ferrite) > 1605B (bainite/ferrite) ≥ 1605A (pearlite/ferrite).
2. The rust layers of LAS with high chromium content (1605A/B) were denser and could therefore provide better protection after longer periods of wet/dry cyclic corrosion. On the other hand, LASs with ultra-low carbon content (1604A/B) have even lower corrosion rates at earlier stages of accelerated corrosion.
3. The mechanical properties of the steels were degraded by corrosion partly because of the reduction in cross-section and partly because of the increase in surface roughness. The degree of degradation was least for SS400.
4. he copper and chromium additions to each steel can enrich the rust-layer/substrate interface and the rust layers, respectively. They can therefore enhance the compactness and densification of these rust layers. In chloride-containing environments, chromium should create a better densification of the rust layers.

5.Combining the results of the accelerated tests and the rust layer analysis, low-alloy steels such as 1605A and 1605B seem to be more suitable for use in the humid and salty weather than Acr-Ten A.

References

1. H. Okada, Y. Hosoi, and H. Naito, Corrosion, 26 (1970) 429.
2. B. R. De Meybaum and E. S. Ayllon, Corrosion, 36 (1980) 345.
3. I. Suzuki, Y. Hisamatsu, and N. Masuka, J. Electrochem. Soc., 127 (1980) 345.
4. H. Schmitter and H. Bohni, J. Electrochem. Soc., 127 (1980) 15.
5. M. Stratman, K. Bohnenkamp, and T. Ramchandran, Corros. Sci., 27 (1987) 905.
6. T. Misawa, K. Asami, K. Hashimoto, and S. Shimodaria, Corros. Sci., 14 (1974) 279.
7. H. Shirasawa, K. Mionoya, H. Tomari, and T. Nakayama, Kobelco Tech. Rev., 12 (1991) 44.
8. J. C. Hudson and J. F. Stanners, J. Iron St. Inst., 180 (1955) 271.
9. C. P. Larrabee and S. K. Coburn, Proc. 1st Cong. Metallic Corrosion, ed. L. Kenwoothy (London, England: Butterworths, 1961), pp. 276-285.
10. E. Williams and M. Komp, Corrosion, 21 (1965) 9.
11. C. Southwell and A. Alexander, Mater. Prot., 9 (1970) 14.
12. H. C. Shih, J. C. Oung, J. T. Wu, and F. I. Wei, Mater. Chem. Phys., 37 (1994) 230.
13. H. H. Uhlig and R. W. Revie, in：Corrosion and Corrosion Control, 3rd ed., J. Wiley & Sons, New York (1991).
14. T. Misawa, K. Hishimoto, and S. Shimodaria, Corros. Sci., 14 (1974) 131.
15. M. Pourbaix and A. Pourbaix, Corrosion, 45 (1989) 71.
16. ASTM E 8M-98, “Standard Test Methods for Tension Testing of Metallic Materials [Metric]”, (1998).
17. ASTM G 50-76 (1992), “Practice for Conducting Atmospheric Corrosion Tests on Metals” (West Conshohocken, PA: ASTM, 1992).
18. ASTM B 117-97, ”Standard Practice for Operating Salt Spray (Fog) Apparatus” (1997).
19. J. H. Wang, F. I. Wei, and H. C. Shih, Corrosion, 52 (1996) 900.
20. J. Davalos, M. Garcia, J. F. Macro, and J. R. Gancedo, Hyperfine Interactions, 69 (1991) 871.
21. ASTM G 1-88, “Standard Practice for Preparing, Cleaning, and Evaluating Corrosion Test Specimens” (1988).
22. S. Feliu and M. Morcillo, Corros. Sci., 34 (1993) 403.
23. R. A. Legault and A. G. Preban, Corrosion, 31 (1975) 117.
24. Jaroslav Kocich, Corros. Sci., 35 (1993) 1.
25. T. Misawa, T. Kyuno, W. Suetaka, and S. Shimodaria, Corros. Sci., 11 (1971) 35.
26. K. Asami and M. Kikuchi, Corros. Sci., 45 (2003) 2671.
27. Y. Hisamatsu and B. Gijutsu, Corros. Eng., 20 (1971) 207.
28. T. Uno and S. Kado, Bull. Jpn. Inst. Met., 10 (1971) 208.
29. K. A. Chandler J. E. Stanners, Proc. 2nd International Congress on Metallic Corrosion, New York, NACE, Houston, Texas, (1963): pp. 325.
30. J. E. Hiller, Wekstoffe u. Korrosion, 17 (1966) 943.
31. P. Keller, Wekstoffe u. Korrosion, 18 (1967) 865.
32. U. R. Evans, Corros. Sci., 9 (1969) 813.
33. J. Keiser, C. Brown, and R. Heidersbach, Corros. Sci., 23 (1983) 251.
34. K. J. Irvine, T. Gladman, and F. B. Pickering, J.

Iron St. Inst., 205 (1967) 161.
35. M. Yamashita, H. Miyuki, Y. Matsuda, H. Magano, and T. Misawa, Corros. Sci., 36 (1994) 283.
36. M. Stratmann, K. Bohnenkamp, and T. Ramchandran, Corros Sci., 27 (1987). 905.
37. Q. C. Zhang, J. S. Wu, J. J. Wang, W. L. Zheng, J. G. Chen, and A. B. Li, Mater. Chem. Phys., 77 (2002) 603.

收到日期：2004 年 10 月 27 日
接受日期：2005 年　3 月 29 日

表1　　測試材料的化學組成 (wt%)。
Table 1　Chemical compositions of the test materials (wt%).

Steel	Fe	C	Si	Mn	P	S	Cu	Ni	Cr	Al	N	Ti
1604A	Bal.	0.01	0.008	1.19	0.06	0.008	0.31	0.16	--	0.033	0.0028	0.023
1604B	Bal.	0.011	0.008	1.19	0.091	0.008	0.30	0.16	--	0.029	0.0028	0.026
1605A	Bal.	0.091	1.06	1.20	0.092	0.0075	0.30	0.16	0.56	0.030	0.0062	--
1605B	Bal.	0.091	1.05	1.20	0.091	0.0075	0.30	0.16	0.56	0.030	0.0062	--
Acr-Ten A	Bal.	0.10	0.44	0.47	0.10	0.008	0.31	0.30	0.55	0.020	--	--
SS400	Bal.	0.13	0.19	0.81	0.015	0.008	0.063	0.049	0.021	0.024	--	--

表2　　在循環加速之後各鋼材對方程式 (1) 的線性回歸係數。
Table 2　Linear regression coefficients of equation (1) for the steel samples after the cyclic accelerated corrosion tests.

Coefficient\Steels	SS400	Acr-Ten A	1604A	1604B	1605A	1605B
X	1.2599	2.1171	1.3450	1.2264	2.1893	2.6981
Y	1.2709	1.1422	1.1956	1.2209	1.0636	1.0239
R2	0.9986	0.9836	0.9864	0.9942	0.9773	0.9784

表3　各鋼材在經過 45 週期的加速試驗之後其機械強度、重量損失和剩餘截面積比的比較。

Table 3　Comparisons of mechanical strength, weight loss, and remaining cross-section after 45 cycles of accelerated corrosion tests.

Steel	SS400	Acr-Ten A	1604A	1604B	1605A	1605B
Weight loss (mg/cm^2)	165.4	187.3	132.4	132.8	147	153.8
Thickness loss (μm) [a]	420.8	476.6	336.9	337.9	374	391.3
Remaining cross-section ratio [b]	0.905	0.908	0.899	0.901	0.901	0.893
Yield strength ratio [c]	0.892	0.853	0.770	0.793	0.780	0.831
Ultimate tensile strength ratio [d]	0.889	0.870	0.846	0.832	0.837	0.833

a: Thickness loss = weight loss / [(upper and lower surfaces)×(iron density)] = $\Delta w/2A\rho$

b: Remaining cross-section ratio = weight of the specimen (after the rust is stripped off) / weight of the specimen (without corrosion) (assuming the length of a specimen is not changed by corrosion)

c: Yield strength ratio = YS (45 cycles) / YS (0 cycle)*

d: Ultimate tensile strength ratio = UTS (45 cycles) / UTS (0 cycle)*

*: YS (0 cycle) and UTS (0 cycle) are both the mechanical strengths of an original (un-corroded) specimen.

a: 厚度損失 = 重量損失 ÷ [(試片上、下表面積)×(鐵的密度)] = $\Delta w/2A\rho$。

b: 剩餘截面積比 = 去除銹層之後的試片重量 ÷ 未經腐蝕的試片(原)重量 (假設試片長度不隨腐蝕而改變)。

c: 降伏強度比 = 經過 45 週期加速試驗後的降伏強度 ÷ 試片的原始(0週期)降伏強度。

d: 最大拉伸強度比 = 經過 45 週期加速試驗後試片的最大拉伸強度 ÷ 試片的原始 (0週期) 最大拉伸強度。

*: 降伏強度 (0週期) 和最大拉伸強度 (0週期) 均表示未經腐蝕試驗的試片機械強度。

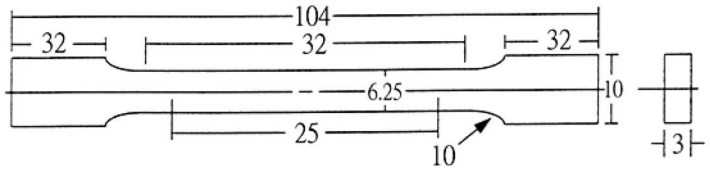

圖1　根據 ASTM E8M 所規範的試片尺寸示意圖，單位為公釐。

Figure 1　Schematic drawings of the test specimen machined according ASTM E8M; dimensions are in mm.

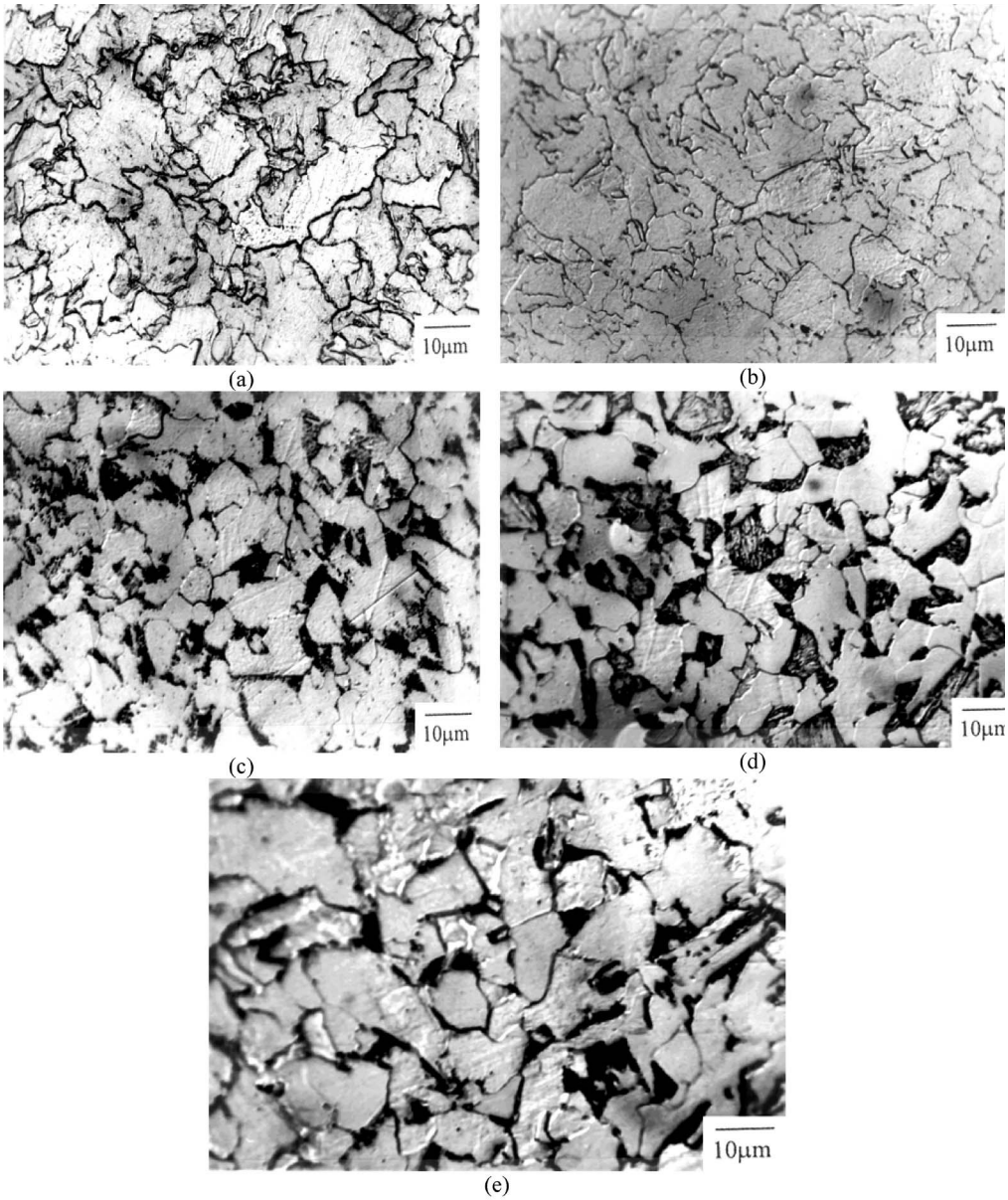

圖2　在掃瞄式顯微鏡下所觀察到的原始 (未經腐蝕試驗) 低合金鋼表面形貌 (放大1000倍)：(a) 1604A、(b) 1604B、(c) 1605A、(d) 1605B 和 (e) Acr-Ten A。

Figure 2　Surface morphology of the as-received low-alloy steels under the scanning electron microscope at a magnification of 1000X: (a) 1604A, (b) 1604B, (c) 1605A, (d) 1605B, and (e) Acr-Ten A.

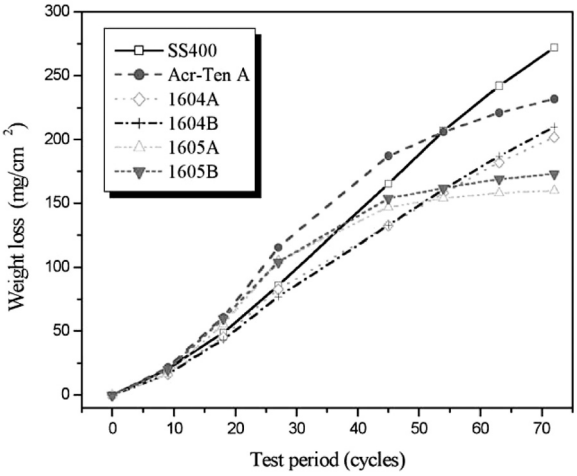

圖3　各鋼材在含氯鹽 (5wt.%) 環境下之重量損失 (毫克/平方公分) 與加速循環腐蝕週期的關係圖。

Figure 3　Relations between the weight loss (mg/cm^2) of the steel samples and the test cycles of accelerated cyclic corrosion in a chloride (5 wt.%) environment.

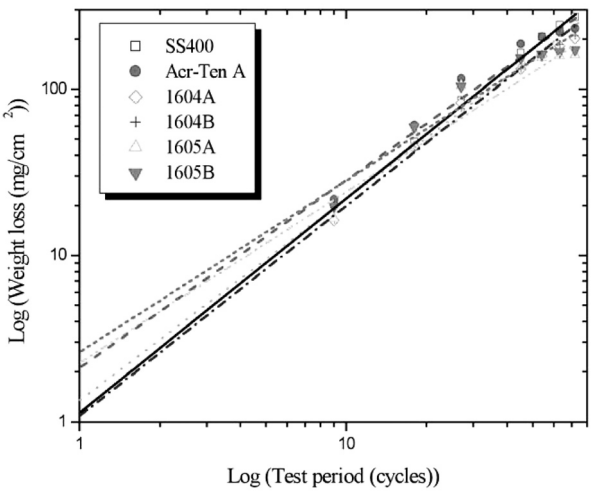

圖4　由圖3 的數據所畫出之重量損失與測試週期的雙對數圖。

Figure 4　Bi-logarithmic plots of data points (weight loss vs. test cycles) from Figure 3.

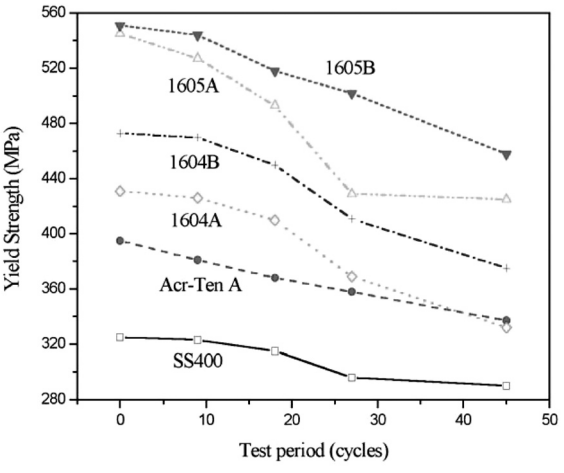

圖5　各鋼材之降伏強度與測試週期的關係圖。

Figure 5　Yield strength of the steels as a function of test cycles.

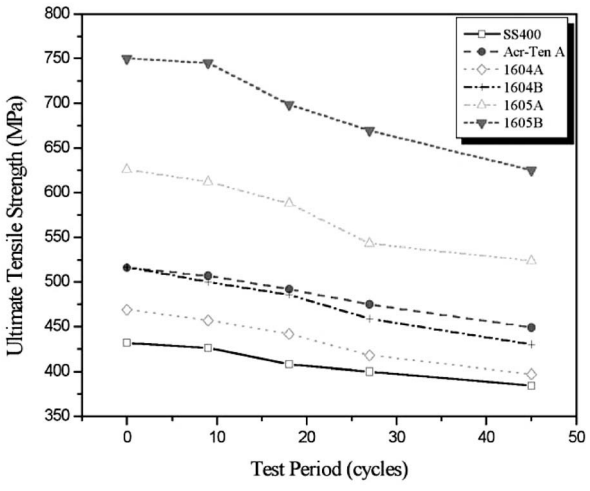

圖6　各鋼材之最大拉伸強度與測試週期的關係圖。

Figure 6　Ultimate tensile strength of the steels as a function of test cycles.

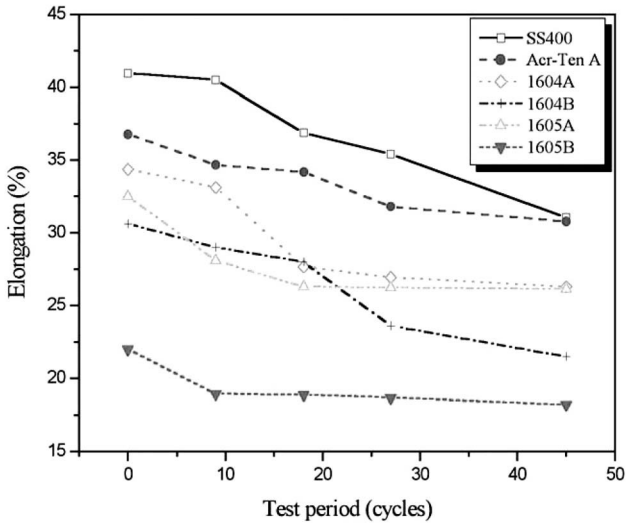

圖7　　各鋼材之延伸率與測試週期的關係圖。

Figure 7　Elongation of the steels as a function of test cycles.

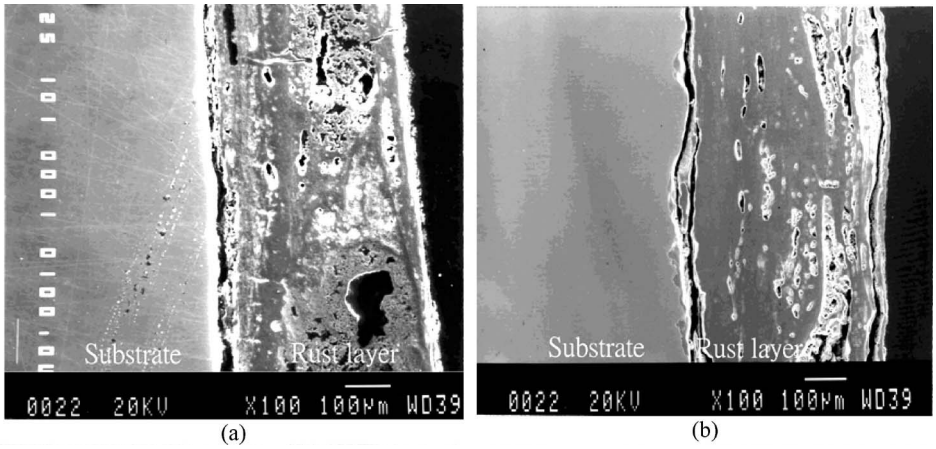

圖8　　各鋼材在分別經過 18 和 45 週期的加速腐蝕試驗後的銹層觀察：(a) SS400 (18週期)、(b) SS400 (45週期)、(c) Acr-Ten A (18週期)、(d) Acr-Ten A (45週期)、(e) 1604A (18週期)、(f) 1604A (45週期)、(g) 1605A (18週期) 和 (h) 1605A (45週期)。

Figure 8　Rust layers on the tested steel samples after 18 and 45 cycles of the accelerated corrosion tests: (a) SS400 (18 cycles), (b) SS400 (45 cycles), (c) Acr-Ten A (18 cycles), (d) Acr-Ten A (45 cycles), (e) 1604A (18 cycles), (f) 1604A (45 cycles), (g) 1605A (18 cycles), (h) 1605A (45 cycles).

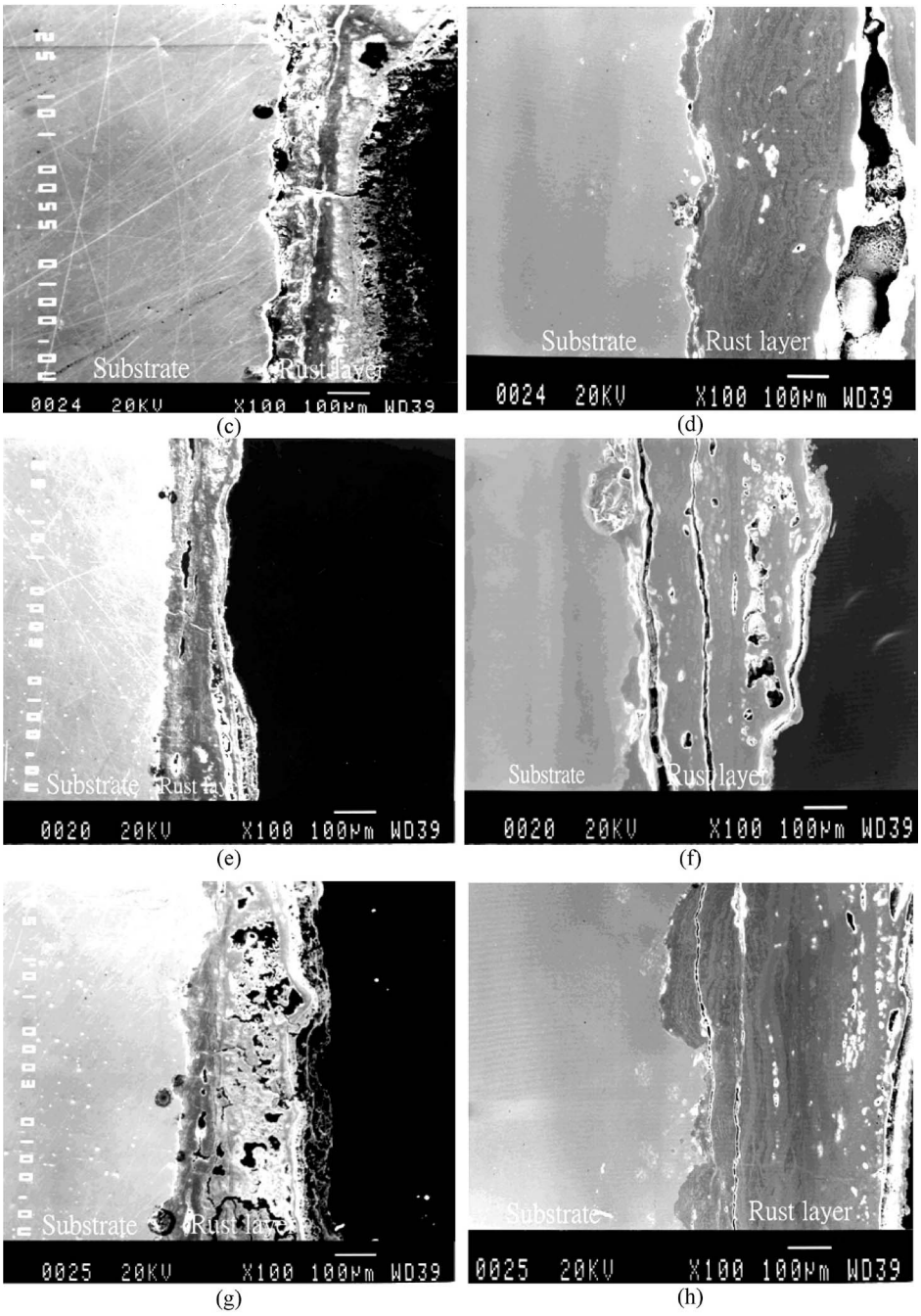

圖8 (續)。
Figure 8 (Cont).

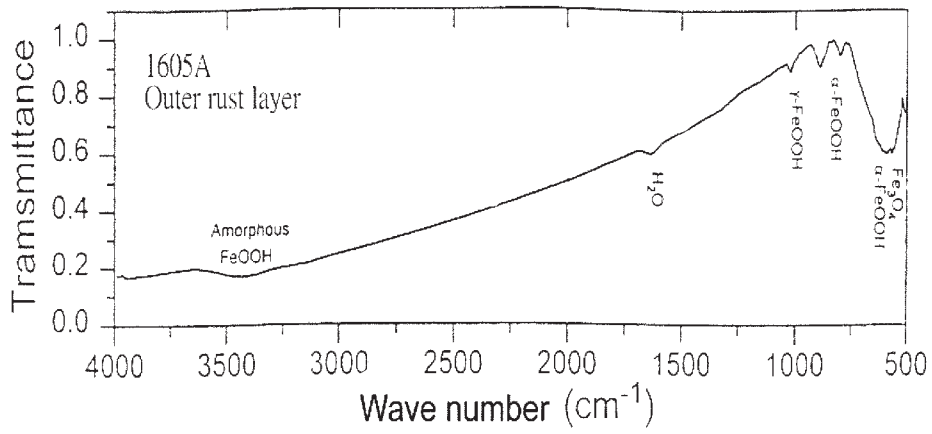

(a)

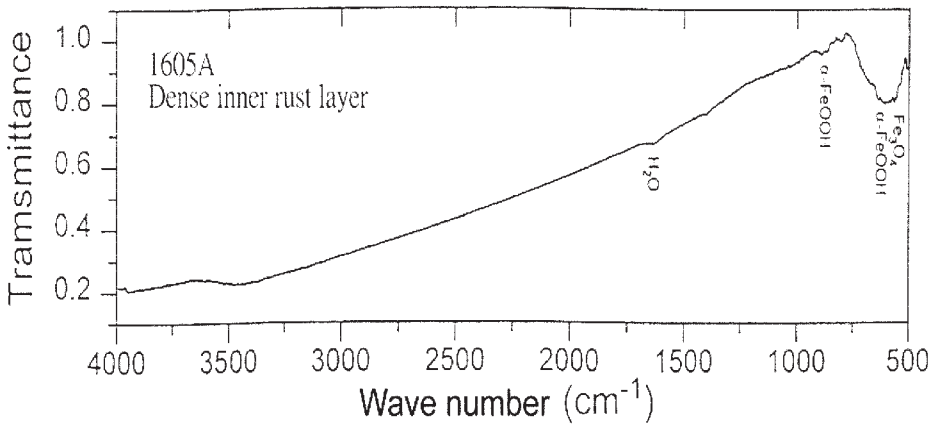

(b)

圖9　各鋼材銹層的 FTIR 光譜圖：(a) 1605A (外銹層)、(b) 1605A (緻密內銹層)、(c) 1605A (表層)、(d) 1604A (外銹層)和(e) 1604A (內銹層)。

Figure 9　FTIR spectrums of the rust layers of the tested steels: (a) 1605A (outer layer), (b) 1605A (dense inner layer), (c) 1605A (surface layer), (d) 1604A (outer layer), (e) 1604A (inner layer).

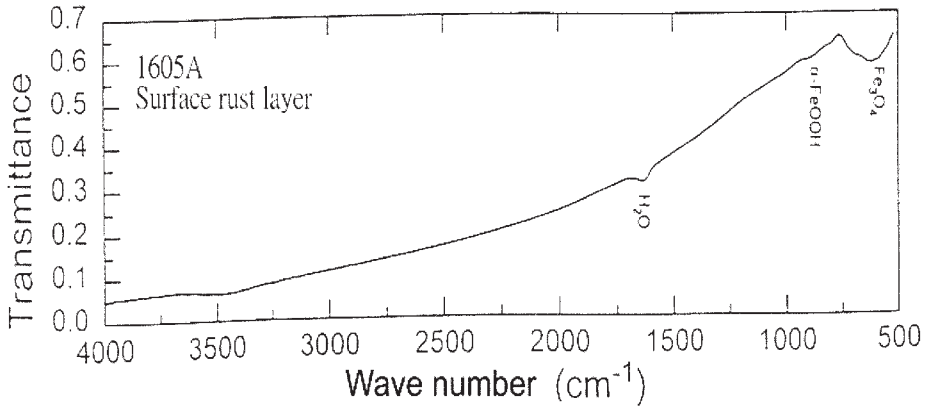

(c)

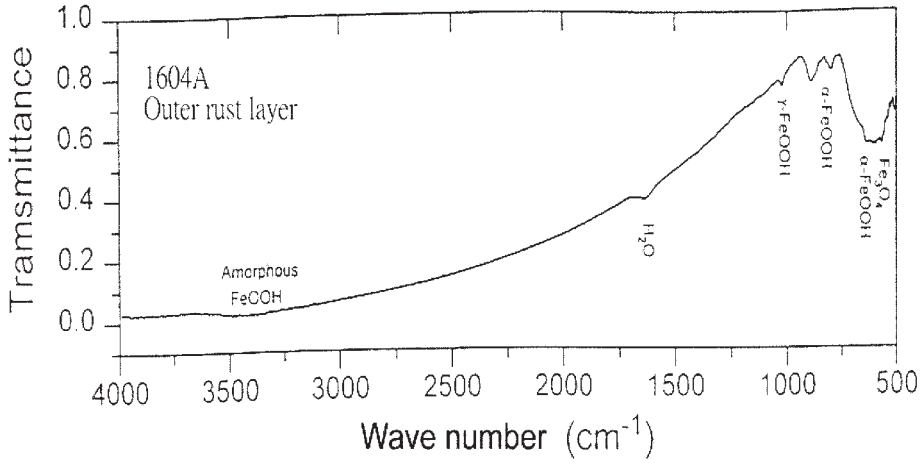

(d)

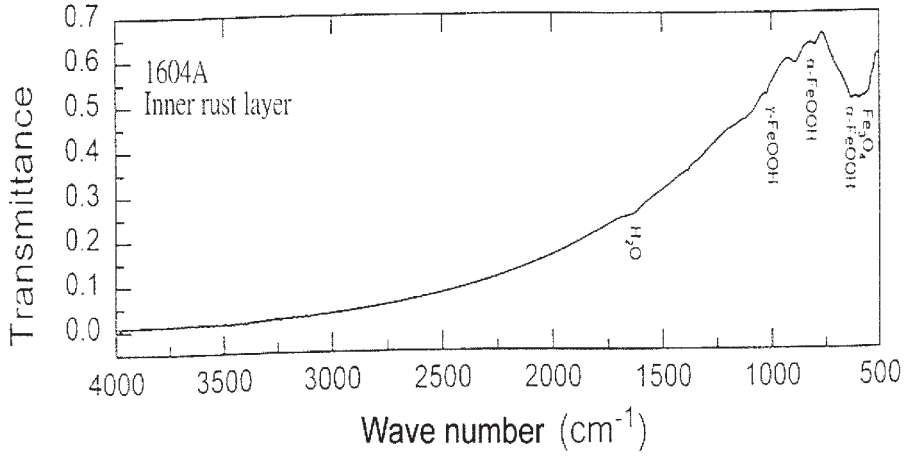

(e)

圖9　(續)。
Figure 9　(Cont).

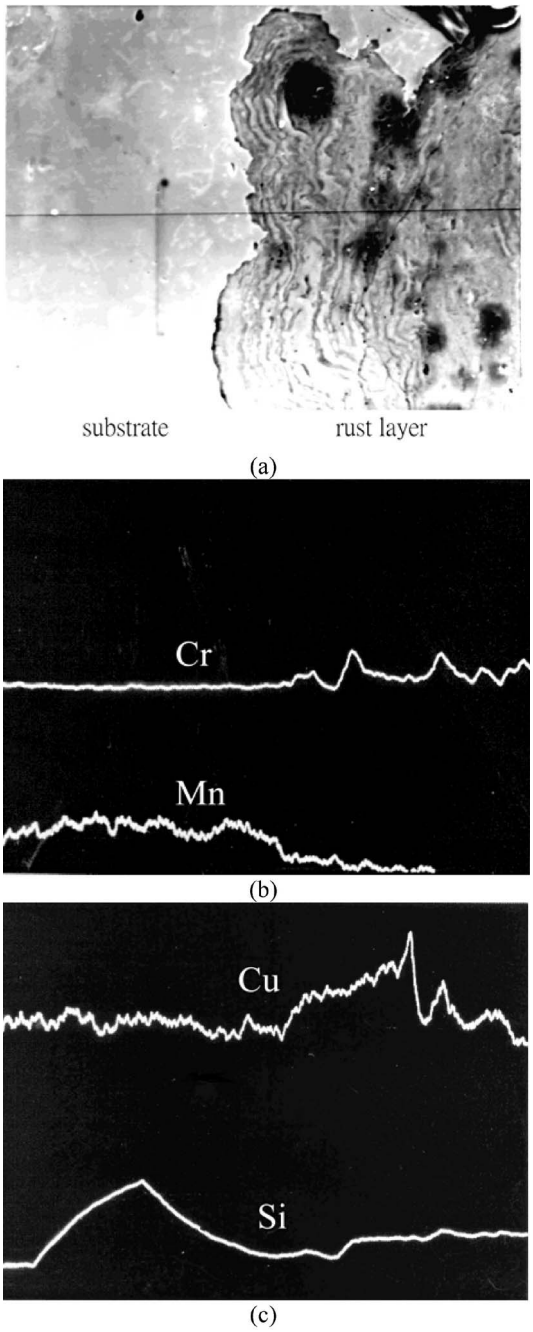

圖10　Acr-TenA 經由 EPMA 分析後在銹層與基材介面的元素線剖面圖：(a) SEM 照片、(b) 鉻與錳、(c) 銅與矽。

Figure 10　EPMA line profiles of the rust layer / substrate for Acr-Ten A: (a) SEM photograph, (b) Cr and Mn, (c) Cu and Si.

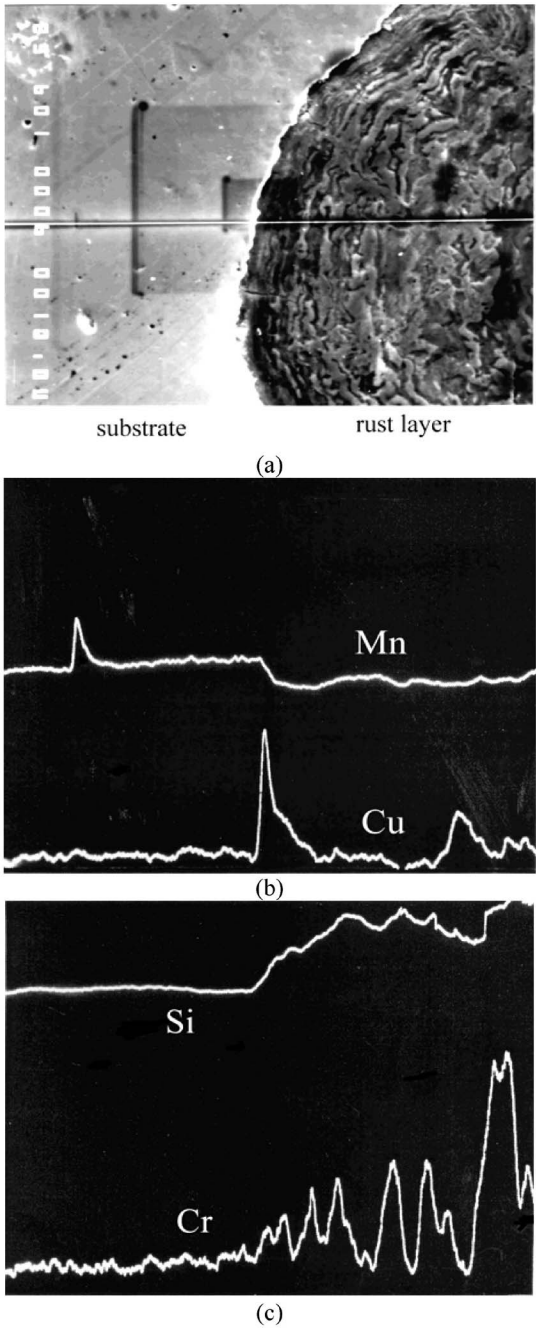

圖11　1605A 經由 EPMA 分析後在銹層與基材介面的元素線剖面圖：(a) SEM 照片、(b) 銅與錳、(c)鉻與矽。

Figure 11　EPMA line profiles of the rust layer / substrate for 1605A: (a) SEM photograph, (b) Cu and Mn, (c) Cr and Si.